Hard Synchrotron Spectra from Magnetically Dominated Plasma Turbulence

Luca Comisso , Emanuele Sobacchi, and Lorenzo Sironi
Department of Astronomy and Columbia Astrophysics Laboratory, Columbia University, New York, NY 10027, USA; luca.comisso@columbia.edu,
es3808@columbia.edu, lsironi@astro.columbia.edu

Abstract

Synchrotron emission from astrophysical nonthermal sources usually assumes that the emitting particles are isotropic. By means of large-scale two- and three-dimensional particle-in-cell simulations, we demonstrate that the dissipation of magnetically dominated ($\sigma_0 \gg 1$) turbulence in pair plasmas leads to strongly anisotropic particle distributions. At Lorentz factors $\sim \sigma_0 \gamma_{th0}$ (here, γ_{th0} is the initial Lorentz factor), the particle velocity is preferentially aligned with the local magnetic field; instead, the highest energy particles are preferentially oriented in the plane perpendicular to the field. This energy-dependent anisotropy leads to a synchrotron spectral flux $\nu F_\nu \propto \nu^s$ that is much harder than for isotropic particles. Remarkably, for $\sigma_0 \gg 1$ we find that the angle-integrated spectral slope in the slow cooling regime is $s \sim 0.5 - 0.7$ for a wide range of turbulence fluctuations, $0.25 \lesssim \delta B_{rms0}^2 / B_0^2 \lesssim 4$, despite significant variations in the power-law energy spectrum of nonthermal particles. This is because weaker turbulence levels imprint a stronger degree of anisotropy, thereby counteracting the effect of the steeper particle spectrum. The synchrotron spectral slope may be even harder, $s \gtrsim 0.7$, if the observer is in the plane perpendicular to the mean magnetic field. Our results are independent of domain size and dimensionality. Our findings may help explain the origin of hard synchrotron spectra of astrophysical nonthermal sources, most notably the radio spectrum of pulsar wind nebulae.

Unified Astronomy Thesaurus concepts: High energy astrophysics (739); Plasma astrophysics (1261); Particle astrophysics (96); Plasma physics (2089); Non-thermal radiation sources (1119); Pulsars (1306)

1. Introduction

Synchrotron emission from a nonthermal population of energetic particles is invoked to explain the radiative signature of a variety of high energy astrophysical sources. The emitting particles are often assumed to be distributed according to a power law with a slope p in energy, $dN/d\gamma \propto \gamma^{-p}$, and their velocity to be isotropically oriented with respect to the local magnetic field. Under these assumptions, the synchrotron energy flux is a power law in frequency, $\nu F_\nu \propto \nu^s$, with spectral slope $s = (3 - p)/2$ (Rybicki & Lightman 1979).

The *ansatz* of isotropy for the velocity distribution of the synchrotron-emitting particles is based on the assumption that the underlying acceleration mechanism does not imprint strong anisotropies, or that some other process (e.g., plasma instabilities) is capable of isotropizing the distribution on timescales shorter than the particle cooling time (Kulsrud 2005; Longair 2011). In this work, we revisit these commonly adopted assumptions by means of first-principles particle-in-cell (PIC) simulations of particle acceleration in magnetically dominated plasma turbulence.

Recent studies of kinetic turbulence in highly magnetized pair plasmas have shown that nonthermal particle acceleration is a generic by-product of the turbulent energy cascade (Zhdankin et al. 2017, 2018; Comisso & Sironi 2018, 2019; Nättilä 2019; Wong et al. 2020). In particular, PIC simulations in unprecedentedly large domains have demonstrated that magnetic reconnection within the turbulent cascade is responsible for the initial particle energization, while large-scale turbulent fluctuations control the acceleration to higher energies (Comisso & Sironi 2018, 2019). A crucial outcome of this energization mechanism is the generation of strongly anisotropic particle distributions (Comisso & Sironi 2019). Hence,

one would expect the synchrotron emission of the turbulence-accelerated particles to deviate significantly from the standard expectation of an isotropic particle population.

In this paper, we quantify the energy dependence of particle anisotropy in magnetically dominated pair plasma turbulence, and we investigate its implications for the synchrotron emission. We show that the self-consistent generation of anisotropic particle distributions gives rise to hard (i.e., $s > 0.5$) synchrotron spectra across an extended frequency range even when the underlying particle spectra are relatively soft (i.e., $p > 2$). Remarkably, the synchrotron slope is nearly insensitive to the degree of initial turbulent fluctuations: weaker turbulence levels produce a stronger anisotropy, thereby counteracting the effect of the softer particle spectrum. Our findings may help explain the origin of the hard radio spectra of pulsar wind nebulae without the need to invoke hard ($p < 2$) particle distributions.

2. Analytical Estimates

We provide a simple analytical estimate of the synchrotron spectrum emitted by an anisotropic population of nonthermal particles (see also Appendix A of Tavecchio & Sobacchi 2020). We assume that the number of particles per unit Lorentz factor is

$$\frac{dN}{d\gamma} \propto \gamma^{-p} \quad \text{for} \quad \gamma_{min} < \gamma < \gamma_{max}, \qquad (1)$$

and that the pitch angle (i.e., the angle α between the particle velocity and the local magnetic field) depends on the particle
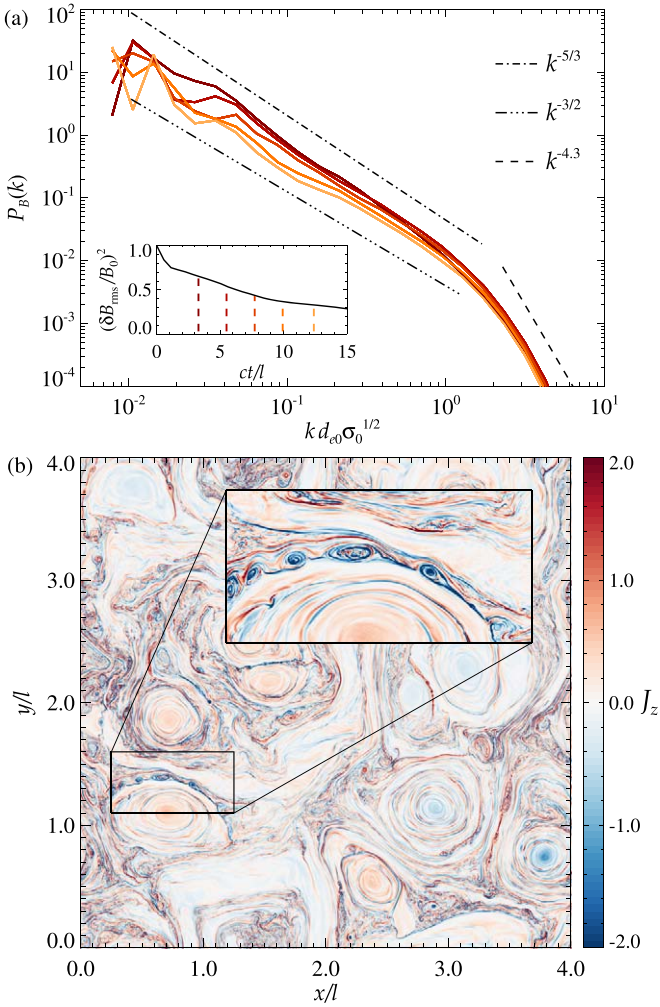
Figure 1. Development of turbulence from a simulation with $\sigma_0 = 75$, $\delta B_{\mathrm{rms}0}/B_0 = 1$, and $L/d_{e0} = 8160$ (with $l = L/4$). Top panel: power spectrum of the magnetic field computed at different times, as indicated by the vertical dashed lines (same color coding) in the inset, which shows the time evolution of $\delta B_{\mathrm{rms}}^2 = \langle \delta B^2 \rangle$ normalized to B_0^2. Bottom panel: out-of-plane current density J_z at $ct/l = 4.4$ (normalized to en_0c) indicating the presence of current sheets and reconnection plasmoids (see the inset).

Lorentz factor as

$$\sin \alpha = \begin{cases} \left(\dfrac{\gamma}{\gamma_{\mathrm{crit}}}\right)^q & \text{for} \quad \gamma_{\min} < \gamma < \gamma_{\mathrm{crit}}, \\ 1 & \text{for} \quad \gamma_{\mathrm{crit}} < \gamma < \gamma_{\max} \end{cases} \qquad (2)$$

with $q > 0$. This assumption is consistent with the results of first-principles PIC simulations of magnetically dominated turbulent plasmas (Comisso & Sironi 2019), where it was shown that the velocity of low energy particles is preferentially aligned with the local magnetic field, while the most energetic particles are preferentially oriented in the plane perpendicular to the field. The origin of the anisotropy is linked to the acceleration mechanism that dominates for particles of a given energy. Particles at the low energy end of the nonthermal tail ($\gamma_{\min} < \gamma < \gamma_{\mathrm{crit}}$, with $\gamma_{\mathrm{crit}} \sim 10\,\gamma_{\min}$) are primarily accelerated by nonideal electric fields aligned with the local magnetic field during reconnection, while the acceleration to larger Lorentz factors ($\gamma_{\mathrm{crit}} < \gamma < \gamma_{\max}$) is controlled by scattering off

turbulent fluctuations, and therefore by electric fields perpendicular to the local magnetic field (Comisso & Sironi 2018, 2019).

We characterize the synchrotron spectrum through the energy flux, νF_ν. For the sake of simplicity, we assume that the magnetic field is a constant, B_0. For electrons with a Lorentz factor $\gamma < \gamma_{\mathrm{crit}}$, the emitted synchrotron frequency is $\nu \sim \gamma^2 \nu_L \sin \alpha \propto \gamma^{2+q}$, where $\nu_L = eB_0/2\pi mc$ is the nonrelativistic Larmor frequency. The photon energy flux is equal to the number of electrons at a given γ, $N_\gamma \sim \gamma(dN/d\gamma) \propto \gamma^{1-p}$, multiplied by the power radiated by one electron, $P_{\mathrm{sync}} = 2\sigma_{\mathrm{T}} c (B_0^2/8\pi)\gamma^2 \sin^2 \alpha \propto \gamma^{2+2q}$, with σ_{T} indicating the Thomson cross section. So when $\gamma < \gamma_{\mathrm{crit}}$, we have $\nu F_\nu \sim N_\gamma P_{\mathrm{sync}} \propto \gamma^{3-p+2q} \propto \nu^{(3-p+2q)/(2+q)}$, and we eventually find that

$$\nu F_\nu \propto \nu^{\frac{3-p}{2}} \times \begin{cases} \left(\dfrac{\nu}{\nu_{\mathrm{crit}}}\right)^{\frac{q(1+p)}{2(2+q)}} & \text{for} \quad \nu_{\min} < \nu < \nu_{\mathrm{crit}}, \\ 1 & \text{for} \quad \nu_{\mathrm{crit}} < \nu < \nu_{\max} \end{cases} \qquad (3)$$

where $\nu_{\min} \sim \gamma_{\min}^2 \nu_L (\gamma_{\min}/\gamma_{\mathrm{crit}})^q$, $\nu_{\mathrm{crit}} \sim \gamma_{\mathrm{crit}}^2 \nu_L$, and $\nu_{\max} \sim \gamma_{\max}^2 \nu_L$. Note that $\nu_{\min}$ is lower by a factor of $(\gamma_{\min}/\gamma_{\mathrm{crit}})^q$ than in the isotropic case $q = 0$.

An anisotropic pitch angle distribution can significantly harden the synchrotron spectrum. Assuming, for example, that $q = p - 1$, Equation (3) gives $\nu F_\nu \propto \nu$ for $\nu_{\min} < \nu < \nu_{\mathrm{crit}}$, and the usual $\nu F_\nu \propto \nu^{(3-p)/2}$ for $\nu_{\mathrm{crit}} < \nu < \nu_{\max}$. Since typically $p \geqslant 2$, the energy flux for $\nu_{\mathrm{crit}} < \nu < \nu_{\max}$ scales as $\nu F_\nu \propto \nu^{1/2}$ or softer. The fact that p and q are correlated is clearly seen in PIC simulations (see below).

3. Numerical Method and Setup

In order to study the development of nonthermal particle acceleration and the associated synchrotron spectrum from magnetically dominated plasma turbulence, we perform ab initio PIC simulations employing the PIC code TRISTAN-MP (Buneman 1993; Spitkovsky 2005). We conduct a suite of large-scale two-dimensional simulations (2D) and one large-scale three-dimensional (3D) simulation. In 2D our computational domain is a square of size L^2, while in 3D it is a cube of size L^3. We use periodic boundary conditions in all directions. For both 2D and 3D domains, all three components of particle momenta and electromagnetic fields are evolved in time. The effect of synchrotron cooling on the particle motion is neglected in all the simulations, which is valid as long as the cooling time of the highest energy particles is much longer than the lifetime of the system.

The simulation setup is similar to our previous works on magnetically dominated plasma turbulence (Comisso & Sironi 2018, 2019). We initialize a uniform electron–positron plasma with total particle density n_0 according to a Maxwell–Jüttner distribution $f(\gamma) \propto n_0 \sqrt{\gamma^2 - 1}\, e^{-\gamma/\theta_0}$ with thermal spread $\theta_0 = k_{\mathrm{B}} T_0/mc^2 = 0.3$, where k_B indicates the Boltzmann constant and T_0 is the initial plasma temperature. The corresponding mean particle Lorentz factor at the initial time is $\gamma_{\mathrm{th}0} \simeq 1.58$. Turbulence develops from uncorrelated magnetic field fluctuations that are initialized in the plane perpendicular to a uniform mean magnetic field, which is taken along the z-direction, $B_0\hat{z}$. The initial fluctuations have low wavenumbers $k_j = 2\pi n_j/L$, with $n_j \in \{1,\ldots,4\}$ and j indicating the

wavenumber direction, and equal amplitude per mode. With this choice, the initial magnetic energy spectrum peaks near $k_p = 8\pi/L$, which defines the energy-carrying scale $l = 2\pi/k_p$ used as our unit length.

The strength of the initial magnetic field fluctuations is parameterized by the magnetization $\sigma_0 = \delta B_{\mathrm{rms0}}^2/4\pi h_0$, where $\delta B_{\mathrm{rms0}} = \langle \delta B^2(t=0)\rangle^{1/2}$ is the space-averaged rms value of the initial magnetic field fluctuations and h_0 is the initial enthalpy density. Here we focus on the magnetically dominated regime, corresponding to $\sigma_0 \gg 1$. We use a fiducial magnetization $\sigma_0 = 75$. Our results do not depend on the choice of the initial thermal spread θ_0, apart from an overall energy rescaling (see Comisso & Sironi 2019).

The large size of our computational domain (with L up to 32640 cells in 2D and 2460 cells in 3D) allows us to achieve asymptotically converged results. We resolve the initial plasma skin depth $d_{e0} = c/\omega_{p0} = \sqrt{\gamma_{\mathrm{th0}}mc^2/4\pi n_0 e^2}$ with 2 cells in 2D and 1.5 cells in 3D. The reference simulation (see Figures 1 and 2) has 64 computational particles per cell on average, while other simulations employ 16 particles per cell, as we have verified that this still properly captures the particles spectrum and anisotropy. The simulation time step is controlled by the numerical speed of light of 0.45 cells per time step.

4. Results

In our simulations, the magnetic energy decays in time, as no continuous driving is imposed, and a well-developed inertial range and kinetic range of the turbulence cascade develop within the outer-scale nonlinear timescale. Figure 1(a) shows the time evolution of the magnetic power spectrum $P_B(k)$ from our reference simulation. Each curve refers to a different time (from brown to orange), as indicated by the corresponding vertical dashed lines in the inset, where we present the temporal decay of the energy in turbulent fluctuations $\delta B_{\mathrm{rms}}^2/B_0^2$. At late times, when most of the turbulent magnetic energy has been transferred to the particles, the particle energy density is roughly in equipartition with the total field energy density. The mean particle Lorentz factor increases to $\langle \gamma \rangle \sim \gamma_\sigma = (1 + \sigma_0/2)\gamma_{\mathrm{th0}}$, and the typical plasma skin depth becomes $d_e \sim d_{e0}\sigma_0^{1/2}$ for $\sigma_0 \gg 1$. From Figure 1(a), we can see that at MHD scales ($kd_{e0}\sigma_0^{1/2} \lesssim 1$) the magnetic power spectrum is consistent with a Kolmogorov scaling $P_B(k) \propto k^{-5/3}$ (Biskamp 2003), while the Iroshnikov-Kraichnan scaling $P_B(k) \propto k^{-3/2}$ (Iroshnikov 1963; Kraichnan 1965) is possibly approached at late times. At kinetic scales, the spectrum steepens and approaches $P_B(k) \propto k^{-4.3}$ (Comisso & Sironi 2019).

As shown in Figure 1(b), the turbulent cascade leads to the formation of intense current layers. Many of these layers become prone to fast magnetic reconnection due to the plasmoid instability that kicks in when the layers exceed a critical aspect ratio (Comisso et al. 2016, 2017; Uzdensky & Loureiro 2016). Magnetic reconnection plays a crucial role in extracting particles from the thermal pool and injecting them into the acceleration process (Comisso & Sironi 2018, 2019). This process leaves a signature in the orientation of the particle velocity with respect to the magnetic field, which, as we show below, has important consequences for the emitted synchrotron radiation.

In Figure 2(a), we show the time evolution of the particle spectrum $dN/d\gamma$. As a result of field dissipation, the spectrum shifts to energies much larger than the initial thermal energy. At
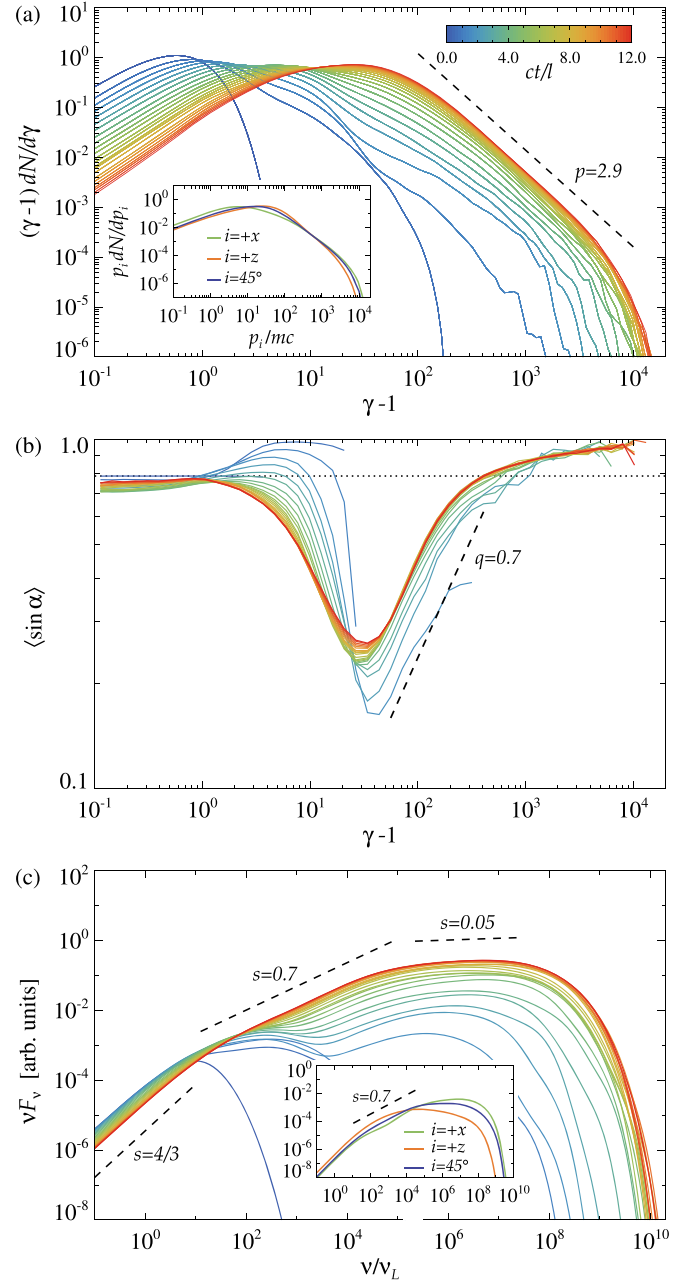

Figure 2. Time evolution of the particle spectrum (top panel), mean pitch angle sine (middle panel), and angle-integrated synchrotron spectrum (bottom panel) for the simulation in Figure 1. The insets of the top and bottom panels show, respectively, the particle momentum spectra and the synchrotron spectra at late times ($ct/l = 11$) along $+\hat{x}$ (green line), $+\hat{z}$ (orange line), and at 45 degrees between $+\hat{x}$ and $+\hat{z}$ (blue line).

late times, when most of the turbulent energy has decayed, the particle energy spectrum stops evolving (orange and red lines), and it peaks at $\gamma \sim 30$. It extends well beyond the peak into a nonthermal tail that can be described by a power law with slope $p = -d\log N/d\log(\gamma - 1) \simeq 2.9$. From the inset in Figure 2(a), we can also see that the momenta of low energy particles are mostly in the direction of the mean magnetic field, while at higher energies, well into the nonthermal tail, particle momenta become mostly perpendicular to it. As we showed in Comisso & Sironi (2018, 2019), this is a consequence of the particle acceleration mechanism: electric fields aligned with the local magnetic field are important at low energies (typical

Lorentz factors up to a few times higher than $\sigma_0\gamma_{th0}$), while electric fields perpendicular to the magnetic field take over at higher energies.

The process of particle acceleration drives a significant energy-dependent anisotropy of the particle pitch angle α, i.e., the angle between the particle velocity and the local magnetic field (see Figures 19–21 in Comisso & Sironi 2019). In particular, in Figure 2(b) we show the average of $\sin\alpha$ as a function of γ. We measure α in the local $\boldsymbol{E} \times \boldsymbol{B}$ frame, since this frame is the appropriate one to compute the synchrotron emission. The measured mean deviates significantly from the expected mean for an isotropic distribution, $\langle\sin\alpha\rangle = \pi/4$ (compare with the dotted line). After a few outer-scale eddy turnover times, $\langle\sin\alpha\rangle$ settles to a steady state. The steady-state curve of $\langle\sin\alpha\rangle$ attains a minimum near the Lorentz factor corresponding to the peak of the particle spectrum at $\gamma \sim \gamma_{th0}\sigma_0/2 \sim 30$, and increases monotonically for higher energies up to $\langle\sin\alpha\rangle \simeq 1$. In particular, in the low energy range of the nonthermal tail, $40 \lesssim \gamma \lesssim 300$, the mean pitch angle sine follows an approximate power law $\langle\sin\alpha\rangle \propto \gamma^q$ with $q \simeq 0.7$. This implies that a particle with $\gamma \sim \gamma_{th0}\sigma_0/2$ will have a significantly weaker synchrotron emission than a particle in the high energy end of the nonthermal tail.

We calculate the synchrotron spectrum by summing over the angle-integrated synchrotron emission from every particle in an incoherent way (Rybicki & Lightman 1979; Reville & Kirk 2010). Figure 2(c) shows the time evolution of the angle-integrated synchrotron spectrum νF_ν.[1] At very low frequencies, $\nu \ll \gamma_\sigma^2 \nu_L \langle\sin\alpha\rangle_{\gamma_\sigma}$, where $\gamma_\sigma = (1 + \sigma_0/2)\gamma_{th0}$ is the post-dissipation mean Lorentz factor and $\langle\sin\alpha\rangle_{\gamma_\sigma}$ is the mean pitch angle sine at γ_σ, the spectrum is the usual $\nu F_\nu \propto \nu^{4/3}$. At very high frequencies, the synchrotron spectrum is $\nu F_\nu \propto \nu^{(3-p)/2} = \nu^{0.05}$, which is consistent with the standard synchrotron spectral slope produced by an isotropic nonthermal particle population with $p = 2.9$. However, there is an intermediate frequency range—extending over nearly four orders of magnitude in frequency— with a harder spectral slope, $\nu F_\nu \propto \nu^{0.7}$, which corresponds to the range where the emitting particles are anisotropic. Indeed, we have verified that the synchrotron spectral slope in this range, $s = 0.7$, is in line with the estimate from Equation (3).

In the inset of Figure 2(c) we show the synchrotron spectrum at late times along different directions, by considering only the particles whose velocity vector falls within a solid angle $\Omega/4\pi = 0.01$ around the line of sight. As expected, the anisotropy of the emitting particles leads to an anisotropic synchrotron emissivity. In the plane perpendicular to the background magnetic field (i.e., along the $+\hat{\boldsymbol{x}}$ direction), the synchrotron spectral slope is even harder than $s = 0.7$. This is due to the fact that (i) high energy particles, which have $\langle\sin\alpha\rangle \sim 1$, emit preferentially in the direction perpendicular to the background field;[2] (ii) low energy particles, which have $\langle\sin\alpha\rangle \ll 1$, emit preferentially in the direction of the background field, and therefore do not contribute to the synchrotron emission along $+\hat{\boldsymbol{x}}$. For a similar reason, the synchrotron spectrum in the $+\hat{\boldsymbol{z}}$ direction of the background field is softer than $s = 0.7$.
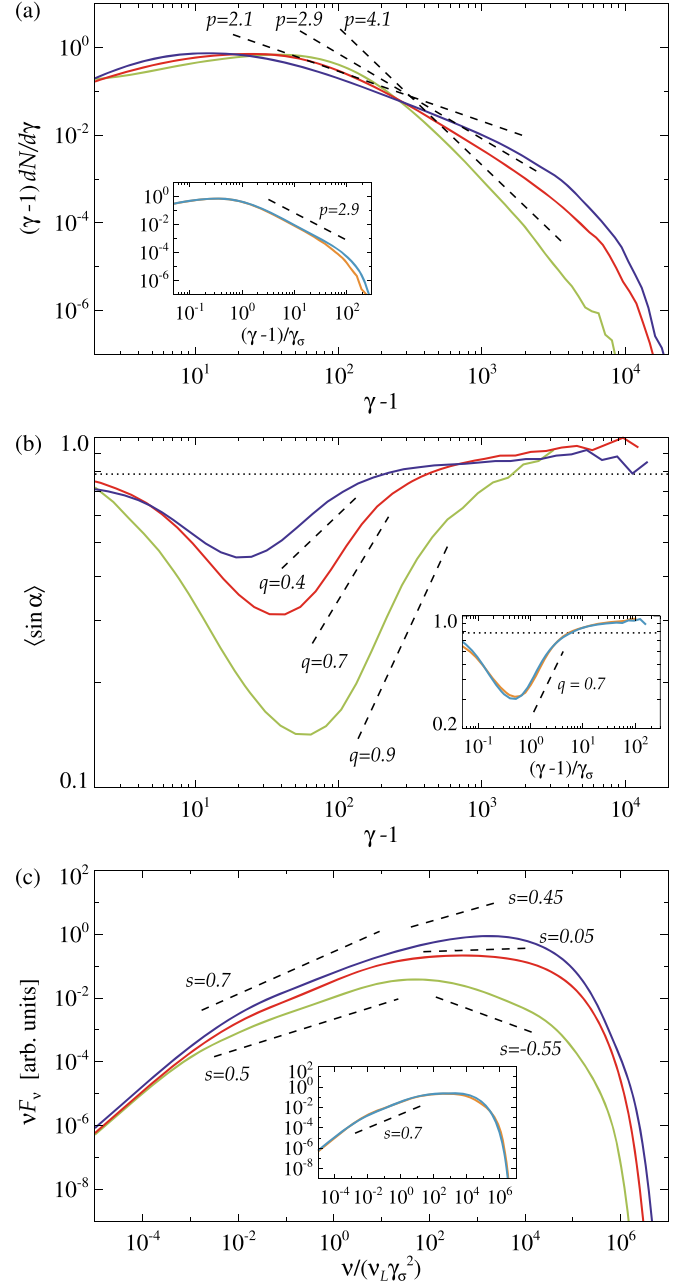
Figure 3. Panels as in Figure 2, for cases with different $\delta B_{\mathrm{rms0}}^2/B_0^2 = 0.25$ (green), 1 (red), and 4 (blue) at late times ($ct/l = 11$). We fix $\sigma_0 = 75$ and $L/d_{e0} = 8160$. The insets show the results from two additional simulations with $\delta B_{\mathrm{rms0}}^2/B_0^2 = 1$, $L/d_{e0} = 8160$, and different magnetization $\sigma_0 = 75/2$ (orange line) and $\sigma_0 = 2 \times 75$ (cyan line).

In order to understand the dependence of the synchrotron spectrum on the main physical parameters that govern the problem, we perform a suite of simulations with different physical conditions. The results from simulations with different values of $\delta B_{\mathrm{rms0}}^2/B_0^2 = 0.25, 1, 4$ are shown in the main panels of Figure 3. A striking result is that in the anisotropy dominated range, the synchrotron spectra νF_ν have very similar slopes (see Figure 3(c)), despite significant differences in the slopes of the particle spectra in Figure 3(a). This is due to the fact that the anisotropy is stronger (i.e., $\langle\sin\alpha\rangle$ reaches lower values) for a weaker level of turbulent fluctuations. Indeed, when the mean magnetic field is stronger, i.e., $\delta B_{\mathrm{rms}}^2/B_0^2$ is smaller, the rate of pitch angle isotropization is lower since the pitch angle

---

[1] We normalize the synchrotron energy flux νF_ν to $P_{\gamma_\sigma} N_p$, where $P_{\gamma_\sigma} = (4/3)c\sigma_T\gamma_\sigma^2 B_0^2/8\pi$ is the mean synchrotron power per particle of an isotropic population with $\gamma = \gamma_\sigma$, while N_p is the total number of particles.

[2] At late times, turbulent magnetic fluctuations have decayed, so the direction of the local magnetic field in the $\boldsymbol{E} \times \boldsymbol{B}$ frame, where the pitch angle should be computed, nearly coincides with the $+\hat{\boldsymbol{z}}$ direction of the background field.
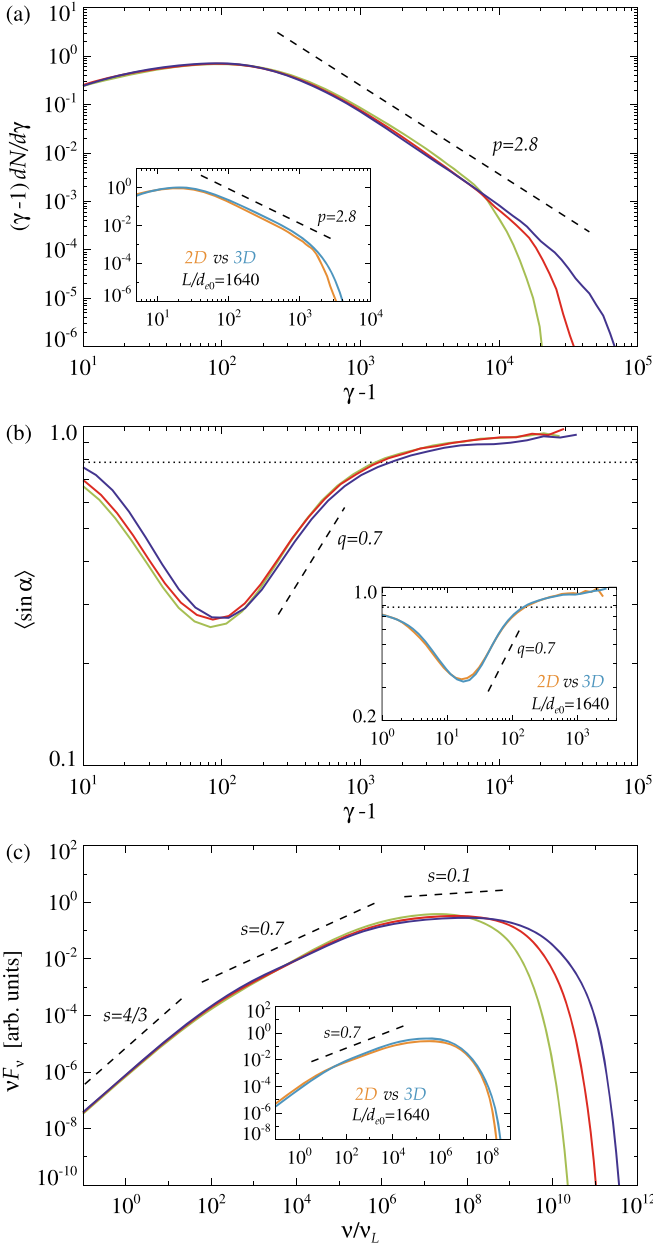
Figure 4. Panels as in Figure 2, for cases with different system size $L/d_{e0} = 4080$ (green), 8160 (red), and 16320 (blue) at late times ($ct/l = 11$). We fix $\delta B_{\mathrm{rms0}}/B_0 = 1$ and $\sigma_0 = 300$. The insets show the comparison between 3D (cyan line) and 2D (orange line) simulations with $\delta B_{\mathrm{rms0}}/B_0 = 1$, $\sigma_0 = 40$, and $L/d_{e0} = 1640$, taken at late times when the residual turbulent magnetic energy in the two simulations is about the same.

scattering timescale is $t_{\mathrm{scatt}} \propto B_0^2/\delta B_{\mathrm{rms}}^2$, which allows the accelerated particles to approach the strongest anisotropy attainable in reconnection. At higher energies, scattering off turbulent fluctuations drives the emitting particles in the direction perpendicular to the local magnetic field (Comisso & Sironi 2018, 2019), and the synchrotron spectrum approaches the expected scaling $\nu F_\nu \propto \nu^{(3-p)/2}$. As shown in the insets, where we investigate the dependence of our results on σ_0, for large values of the magnetization the differences in the particle spectrum and the pitch angle anisotropy are minor, which leads to a synchrotron spectrum with a slope of $s \simeq 0.7$ for both $\sigma_0 = 75/2$ and $\sigma_0 = 2 \times 75$.

In Figure 4 we show the dependence of our results on the system size. As can be seen from Figure 4(a), the particle spectra at late times from simulations with different system size differ only in the extension of the high energy tail, which extends up to the cutoff Lorentz factor $\gamma_{\mathrm{max}} \sim \sqrt{\sigma_z} \gamma_{\mathrm{th0}}(l/d_{e0})$, where $\sigma_z = B_0^2/4\pi h_0 = \sigma_0(B_0^2/\delta B_{\mathrm{rms0}}^2)$ is the magnetization associated with the mean magnetic field (Comisso & Sironi 2018). Figure 4(b) shows that the pitch angle anisotropy remains essentially the same for different domain sizes. This translates directly to the synchrotron spectrum shown in Figure 4(c), which exhibits the same slope of $s \simeq 0.7$ in the anisotropy dominated frequency range, while the high-frequency cutoff increases quadratically with the system size since $\nu_{\mathrm{max}} \sim \gamma_{\mathrm{max}}^2 \nu_L$.

We have shown in Comisso & Sironi (2018, 2019) that the basic ingredients of the synchrotron spectrum, namely the particle spectrum and the characteristic pitch angle, are remarkably similar between 2D and 3D simulations. As a further confirmation, in the insets of Figures 4(a) and 4(b) we show the particle spectrum and the mean pitch angle sine at late times from 3D and 2D simulations with the same physical parameters, which display a remarkable agreement. As a consequence, the synchrotron spectrum computed from the 3D simulation, which is shown in the inset of Figure 4(c) (cyan line), is very close to the one computed from the corresponding 2D simulation (orange line). Again, the angle-integrated synchrotron spectrum displays a slope $s \simeq 0.7$ in the anisotropy dominated frequency range.

5. Discussion

We have shown that the angle-integrated synchrotron spectrum of electrons accelerated by magnetically dominated turbulence can be remarkably hard, $\nu F_\nu \propto \nu^s$ with $s \sim 0.5 - 0.7$, over a range of nearly four orders of magnitude in frequency. The spectral slope may be even harder, $s \gtrsim 0.7$, if the observer is in the plane perpendicular to the mean magnetic field. The spectral hardness does not arise because the particle energy spectrum itself is hard, i.e., $dN/d\gamma \propto \gamma^{-p}$ with $p < 2$, but rather because the distribution is anisotropic. Within the nonthermal tail of accelerated particles, lower energy electrons tend to be more aligned with the local magnetic field than higher energy electrons, so their synchrotron emission is comparatively weaker. This energy-dependent anisotropy has the effect of hardening the synchrotron spectrum.[3]

Our results have important implications for the interpretation of the hard radio spectra of pulsar wind nebulae (PWNe), where the observed radio spectral index is typically $s \sim 0.7 - 1$ (Gaensler & Slane 2006; Reynolds et al. 2017). In the notable case of the Crab Nebula, the radio spectral index is $s \sim 0.7$ (Hester 2008; Bühler & Blandford 2014). Turbulence, which develops as an effect of MHD instabilities in PWNe (Porth et al. 2014), has been suggested to accelerate the radio-emitting electrons (Lyutikov et al. 2019; Xu et al. 2019). However, these studies simply invoked a hard particle spectrum ($p < 2$) over some energy range, without addressing from first principles the origin of the accelerated particles. We

---

[3] We expect similar conclusions to hold for electrons accelerated by reconnection with a strong guide field, even in a nonturbulent environment. Indeed, in our simulations of magnetically dominated turbulence, the acceleration of particles attaining the strongest anisotropy is primarily due to reconnection (Comisso & Sironi 2019). In laminar reconnection, the guide field would play the role of the mean field of our turbulent setup.

have shown that producing hard radio spectra does not necessarily require an acceleration mechanism that transfers most of the available energy to a small fraction of particles (which is the case when $p < 2$). Instead, hard synchrotron spectra may be produced by a relatively soft population of nonthermal particles with an energy-dependent anisotropy. Finally, note that our assumption of neglecting the effect of synchrotron cooling on the particle evolution is well justified in PWNe, where the cooling time of radio-emitting electrons is longer than the age of the system.

For the Crab Nebula, it is generally quoted that the hard spectral slope persists over six orders of magnitude in frequency (for an extended discussion, see, e.g., Bietenholz et al. 1997). Since the hard range of our synchrotron spectra extends over four decades, contributions from turbulent regions with moderately different properties would be required. While a detailed comparison to the Crab Nebula radio emission is left for future work, we mention that in our model we would imply that (i) the total number of radio-emitting electrons is at least one order of magnitude higher than in the case with isotropic electrons. More precisely, the number of radio electrons increases by a factor of $(\nu_{\mathrm{crit}}/\nu_{\mathrm{min}})^{q/(2+q)}$; (ii) the initial magnetization of the plasma is relatively low and/or the predissipation plasma is relatively cold, $\gamma_\sigma \sqrt{\langle \sin \alpha \rangle_{\gamma_\sigma}} \lesssim 10^3$, where $\gamma_\sigma \sim \gamma_{\mathrm{th0}} \sigma_0$ and $\langle \sin \alpha \rangle_{\gamma_\sigma}$ is the mean pitch angle of the electrons at $\gamma \sim \gamma_\sigma$. This constraint comes from the fact that in the Crab $\nu_{\mathrm{min}} \sim \gamma_\sigma^2 \nu_L \langle \sin \alpha \rangle_{\gamma_\sigma} \lesssim$ GHz, and assuming a magnetic field of $B_0 \sim 0.2$ mG.

Anisotropic distributions of the emitting electrons—which we have demonstrated to be a natural by-product of magnetically dominated turbulence (Comisso & Sironi 2019) —have been invoked in other astrophysical sources, including gamma-ray bursts (GRBs) and blazars. In GRBs, anisotropic distributions may explain (i) low-frequency spectra harder than the synchrotron line of death $\nu F_\nu \propto \nu^{4/3}$ in the prompt emission (Lloyd & Petrosian 2000; Lloyd-Ronning & Petrosian 2002; Yang & Zhang 2018); (ii) fast variability (Beloborodov et al. 2011) and some degree of circular polarization (Wiersema et al. 2014; see also Nava et al. 2016) in the afterglow. Some of these models require the electron pitch angle to be $\lesssim 1/\gamma$, which might be possible if the electrons are nonrelativistic before the turbulent component of the magnetic field is dissipated. In blazars, the magnetization of the emission region that is inferred from the spectral modeling may significantly increase if the electron distribution is anisotropic, which is more consistent with the expected magnetic nature of jets (Sobacchi & Lyubarsky 2019, 2020; Tavecchio & Sobacchi 2020). Considering the effect of synchrotron and/or inverse Compton cooling on the electron distribution, as required to model GRBs and blazars, is left for a future study.

ORCID iDs

Luca Comisso ⓘ https://orcid.org/0000-0001-8822-8031

References

Beloborodov, A. M., Daigne, F., Mochkovitch, R., & Uhm, Z. L. 2011, MNRAS, 410, 2422
Bietenholz, M. F., Kassim, N., Frail, D. A., et al. 1997, ApJ, 490, 291
Biskamp, D. 2003, Magnetohydrodynamic Turbulence (Cambridge: Cambridge Univ. Press)
Bühler, R., & Blandford, R. 2014, RPPh, 77, 066901
Buneman, O. 1993, in Computer Space Plasma Physics: Simulation Techniques and Software, ed. H. Matsumoto & Y. Omura (Terra Scientific: Tokyo), 67
Comisso, L., Lingam, M., Huang, Y.-M., & Bhattacharjee, A. 2016, PhPl, 23, 100702
Comisso, L., Lingam, M., Huang, Y. M., & Bhattacharjee, A. 2017, ApJ, 850, 142
Comisso, L., & Sironi, L. 2018, PhRvL, 121, 255101
Comisso, L., & Sironi, L. 2019, ApJ, 886, 122
Gaensler, B. M., & Slane, P. O. 2006, ARA&A, 44, 17
Hester, J. J. 2008, ARA&A, 46, 127
Iroshnikov, P. S. 1963, AZh, 40, 742
Kraichnan, R. H. 1965, PhFl, 8, 1385
Kulsrud, R. M. 2005, Plasma physics for astrophysics (Princeton, NJ: Princeton Univ. Press)
Lloyd, N. M., & Petrosian, V. 2000, ApJ, 543, 722
Lloyd-Ronning, N. M., & Petrosian, V. 2002, ApJ, 565, 182
Longair, M. S. 2011, High Energy Astrophysics (Cambridge: Cambridge Univ. Press)
Lyutikov, M., Temim, T., Komissarov, S., et al. 2019, MNRAS, 489, 2403
Nättilä, J. 2019, arXiv:1906.06306
Nava, L., Nakar, E., & Piran, T. 2016, MNRAS, 455, 1594
Porth, O., Komissarov, S. S., & Keppens, R. 2014, MNRAS, 438, 278
Reville, B., & Kirk, J. G. 2010, ApJ, 724, 1283
Reynolds, S. P., Pavlov, G. G., Kargaltsev, O., et al. 2017, SSRv, 207, 175
Rybicki, G. B., & Lightman, A. D. 1979, Radiative Processes in Astrophysics (New York: Wiley)
Sobacchi, E., & Lyubarsky, Y. E. 2019, MNRAS, 484, 1192
Sobacchi, E., & Lyubarsky, Y. E. 2020, MNRAS, 491, 3900
Spitkovsky, A. 2005, in AIP Conf. Ser., Vol. 801, Astrophysical Sources of High Energy Particles and Radiation, ed. T. Bulik, B. Rudak, & G. Madejski (Melville, NY: AIP), 345
Tavecchio, F., & Sobacchi, E. 2020, MNRAS, 491, 2198
Uzdensky, D. A., & Loureiro, N. F. 2016, PhRvL, 116, 105003
Wiersema, K., Covino, S., Toma, K., et al. 2014, Natur, 509, 201
Wong, K., Zhdankin, V., Uzdensky, D. A., Werner, G. R., & Begelman, M. C. 2020, ApJL, 893, L7
Xu, S., Klingler, N., Kargaltsev, O., & Zhang, B. 2019, ApJ, 872, 10
Yang, Y.-P., & Zhang, B. 2018, ApJL, 864, L16
Zhdankin, V., Uzdensky, D. A., Werner, G. R., & Begelman, M. C. 2018, ApJL, 867, L18
Zhdankin, V., Werner, G. R., Uzdensky, D. A., & Begelman, M. C. 2017, PhRvL, 118, 055103